Mitigating hydrogen embrittlement in CoCrNi alloy using a self-refilling nanoscale amorphous oxide layer

Jiang Yi [a,1], Shuting Zhang [a,b,1], Dingding Zhu [a], Mujin Yang [a], Minglin He [a], Bo Du [a], Shuai Wang [a,*]

[a] Department of Mechanical and Energy Engineering, Southern University of Science and Technology, 1088 Xueyuan Avenue, Shenzhen 518055, PR China
[b] Karlsruhe Institute of Technology (KIT), P.O. Box 3640, Karlsruhe 76021, Germany

Keywords:
Hydrogen embrittlement
Equiatomic alloys
CoCrNi
CoCrNiSi
Oxide-amorphous layer

A B S T R A C T

Designing hydrogen embrittlement-resistant materials exposed to extreme conditions has long been challenging. In this work, we introduced a strategy combining Si alloying with short-term oxidation to generate a nanoscale amorphous layer on CoCrNi alloy. The layer spontaneously formed in a high-temperature environment and was firmly bonded to the matrix. This nanoscale amorphous layer reduced the hydrogen penetration rate by 62 %. The hydrogen-charged CoCrNi alloy with amorphous layers still retained a high tensile strength of 890 MPa and a strain-to-failure of 57 %, while the embrittlement sensitivity is only 0.04 (which is 0.25 for bare CoCrNi), demonstrating an outstanding hydrogen embrittlement resistance. The nanoscale amorphous layer is an effective hydrogen barrier due to its dense structure, which lacks rapid hydrogen diffusion pathways such as dislocations and grain boundaries. Additionally, the amorphous layer reduces Cr depletion at subsurface grain boundaries and prevents the formation of pores induced by the Kirkendall effect. Compared to traditional coatings, the amorphous layer can be self-refilled at critical temperature after damage under external loading. This approach provides a long-run approach for designing hydrogen embrittlement-resistant alloys capable of withstanding extreme service conditions.

1. Introduction

Structural components used in nuclear energy, oil, and petrochemical processing are often exposed to harsh conditions where high hydrogen concentrations, elevated temperatures, and oxidation coexist [1,2]. Compared to other damage mechanisms like oxidation and corrosion, which are visible to the naked eye, hydrogen embrittlement is more difficult to prevent due to its persistent, concealed, and unpredictable nature, posing a great threat to the service life of materials[3].

Since the discovery of hydrogen embrittlement 150 years ago, numerous researchers have focused on exploring its mechanisms and prevention strategies[2–5]. However, current hydrogen embrittlement mitigation strategies fail to fully meet demands for severe operating conditions. Currently, there are two main approaches in the field[6]: (1) Intrinsic hydrogen resistance is enhanced through compositional and process design, such as by adding precipitate phases to create irreversible hydrogen traps[7,8]. However, this approach complicates the manufacturing process, and the introduced traps can become unstable and ineffective under high-temperature service conditions. Moreover, altering the material's microstructure may compromise its original properties. (2) Extrinsic hydrogen resistance is improved by applying surface treatments like nitriding, carburizing, coating, sputtering, or electroplating, which deposit a hydrogen-resistant layer of FCC metals [9–11], ceramic-based materials[12], nitrides[13], or carbides[14] onto the surface to act as a hydrogen barrier. Nevertheless, these surface treatments often require complex processes and specialized equipment, resulting in potential weak spots in the barrier, especially for components with intricate geometries. Additionally, many of these hydrogen barriers lack a strong metallurgical bond with the substrate, leading to delamination and failure during service.

Therefore, there is an urgent need to develop a more effective hydrogen embrittlement resistance strategy for these extreme conditions. Equiatomic alloys have demonstrated strong potential in fields like mechanics[15–17], electrochemistry[18], and magnetism[19].

* Corresponding author.
E-mail address: wangs@sustech.edu.cn (S. Wang).
[1] These authors contributed equally to this work.

Their sluggish diffusion effect makes them one of the most attractive materials for anti-hydrogen-embrittlement[20]. Alloys such as CoCrNi [21], CoNiV[22], FeCoCrNi[23,24], and FeCoCrNiMn[25] have shown better resistance to hydrogen embrittlement than traditional nickel-based alloys and stainless steels. However, their hydrogen embrittlement resistance under extreme conditions still requires validation and improvement. The mechanisms underlying the hydrogen embrittlement resistance of these alloys have been extensively investigated. Li et al.[23] reported that tuning the Fe content in FeCoCrNi alloys induces Cr segregation at grain boundaries, effectively reducing grain boundary free volume and suppressing hydrogen adsorption, thereby enhancing hydrogen embrittlement resistance. Soundararajan et al.[21] demonstrated that equiatomic CoCrNi alloys retain good ductility under electrochemical hydrogen charging, as hydrogen reduces the stacking fault energy and facilitates the formation of deformation-induced nanotwins. Our previous work [26] showed that incorporating a controlled amount of Mo into equiatomic CoCrNi alloys strengthens the material and promotes deformation twinning, significantly improving hydrogen embrittlement resistance. Luo et al. [22] revealed that equiatomic CoCrV alloys exhibit excellent hydrogen embrittlement resistance due to their low hydrogen diffusivity, the presence of a surface passivation layer that mitigates hydrogen ingress, and the ability of deformation twins to accommodate strain. Notably, most existing studies focus on improving intrinsic hydrogen resistance, while strategies aimed at enhancing extrinsic hydrogen resistance remain largely unexplored.

In this study, we modified equiatomic CoCrNi alloys by adding a certain amount of Si, enabling the spontaneous formation of a strongly bonded, highly effective amorphous hydrogen barrier (AHB) layer under high-temperature oxidation. This AHB layer, dense and free of fast hydrogen diffusion pathways, exhibits excellent hydrogen resistance. In our experiments, this barrier reduced hydrogen uptake in the alloy by 62 %. After enduring hydrogen charging under harsh conditions (25 mA/cm^2 in sulfuric acid solution for 7 days), the alloy retained a high tensile strength of 890 MPa and an impressive elongation of 57 %, with only a 4 % loss in ductility (originally over 25 %). Even when local damage occurs, the AHB layer can be in-situ self-refilling under service conditions. This novel design concept provides a new framework for developing hydrogen embrittlement-resistant alloys capable of long-term performance under extreme conditions where high hydrogen content, elevated temperatures, and oxidation coexist.

2. Materials and methods

2.1. Alloy preparation and sample fabrication

The equiatomic CoCrNi alloy and Si-alloyed CoCrNi alloy, referred to as CoCrNi-Si, were synthesized using a vacuum arc melting process with high-purity metals and silicon (purity $>$ 99.9 %). The nominal atomic composition of the CoCrNi-Si alloy is as follows: Co 30.3 %, Cr 30.3 %, Ni 30.3 %, and Si 9.1 %. The alloys were melted and re-melted five times in a non-consumable vacuum arc melting furnace with a tungsten electrode under a high-purity argon atmosphere to ensure homogeneity in microstructure and composition. The resulting ingots were cast into a copper mold with dimensions of 5 $\times$ 10 $\times$ 100 mm^3 . Post-casting, the ingots underwent homogenization at 1373 K for 5 hours to eliminate macro-segregation, followed by cold rolling along the casting direction, achieving a 90 % reduction in thickness to relieve residual stress and produce equiaxed grains. Tensile specimens were prepared in a flat dog-bone shape with a gauge length of 10 mm and a cross-sectional area of 1.0 $\times$ 3.0 mm^2.

Subsequently, the CoCrNi and CoCrNi-Si alloys were annealed and oxidized at 1173 K in an air atmosphere for 10 and 5 min, followed by air cooling. To facilitate characterization and analysis, samples of both alloys oxidized at 1173 K for 60 minutes were similarly prepared. Supplementary Figure 1 presents the EBSD analysis of the annealed and polished samples, while Supplementary Figure 2 shows the XRD analysis of the alloys before and after oxidation. It can be observed that the CoCrNi-Si and CoCrNi alloys exhibit similar grain sizes and share the same FCC crystal structure. Si primarily exists in the alloy as a solid-solution atom, which is consistent with the findings reported by Liu et al.[26] and Chang et al.[27].

2.2. Hydrogen charging and mechanical testing

Selected oxidized samples were further treated by grinding with silicon carbide papers (600–1500 grit) to evaluate the effect of oxides. Electrochemical hydrogen charging was then performed on samples with and without oxide layers. Continuous cathodic charging was applied at a current density of 25 mA/cm^2 for 7 days in an electrolyte consisting of 0.5 mol/L H_2SO_4 with 50 g/L thiourea. A platinum sheet served as the counter electrode. To prevent hydrogen escape, the charged samples were stored in liquid nitrogen prior to testing and characterization. Post-tensile testing, the hydrogen content in the charged samples was measured using gas chromatograph thermal desorption analysis (GC-TDA), conducted with a temperature ramp rate of 200 K/h from room temperature to 1073 K.

To assess hydrogen embrittlement (HE) susceptibility, hydrogen pre-charging was performed on both oxidized and non-oxidized samples, followed by slow strain rate uniaxial tensile tests at an initial strain rate of $\sim 5 \times 10^{-5}\ s^{-1}$. To ensure data reproducibility, the tensile test for each sample was repeated three times. The susceptibility to HE was quantified by the percentage loss of elongation after fracture (δ_{loss}), calculated as:

$$\delta_{loss}(\%) = \frac{\delta_{Uncharged} \quad \delta_{charged}}{\delta_{uncharged}} \tag{1}$$

2.3. Microstructure characterization

The crystal structures of the oxide layers and the bulk CoCrNi and CoCrNi-Si alloys were examined using X-ray diffraction (XRD) at a scan speed of 2°/min. Grain size analysis was conducted via electron backscatter diffraction (EBSD) using an FEI Apreo2 S Lovac scanning electron microscope (SEM) equipped with an EDAX detector. The morphology of the oxide layer was characterized using the same SEM, while surface composition variations were assessed through energy-dispersive X-ray spectroscopy (EDS). Thin transmission electron microscopy (TEM) foils were extracted using the focused ion beam (FIB) lift-out method on an FEI Helios 600i for high-resolution imaging. TEM was performed using an FEI Talos F200X at an accelerating voltage of 200 kV, providing detailed insights into the internal structure of the oxide layers. Additionally, elemental distribution and phase composition were analyzed through EDS integrated with TEM, enabling precise mapping and identification of elements and phases within the oxide layers.

3. Results

3.1. Formation and microstructure of the AHB layer

The AHB layer was formed on the surface of CoCrNi-Si alloy through a brief oxidation treatment. After 5 min of oxidation at 1173 K in air, a distinct layer was observed on the surface of the CoCrNi-Si alloy (Fig. 1a). Cross-sectional analysis using Focused Ion beam (FIB) technology reveals that even at grain boundaries, the layer and the underlying substrate of the CoCrNi-Si alloy remain dense and intact (Fig. 1b). After 60 min of oxidation, the layer thickens to approximately 0.5 μm while maintaining density (Fig. 1c). In contrast, the CoCrNi alloy shows significant oxide accumulation on its surface, particularly along grain boundaries, after just 10 min of oxidation (Fig. 1d). Pores are already visible beneath the oxide layer at grain boundary regions (Fig. 1e). After 60 min of oxidation, the oxide layer thickens rapidly, exceeding 1 μm in

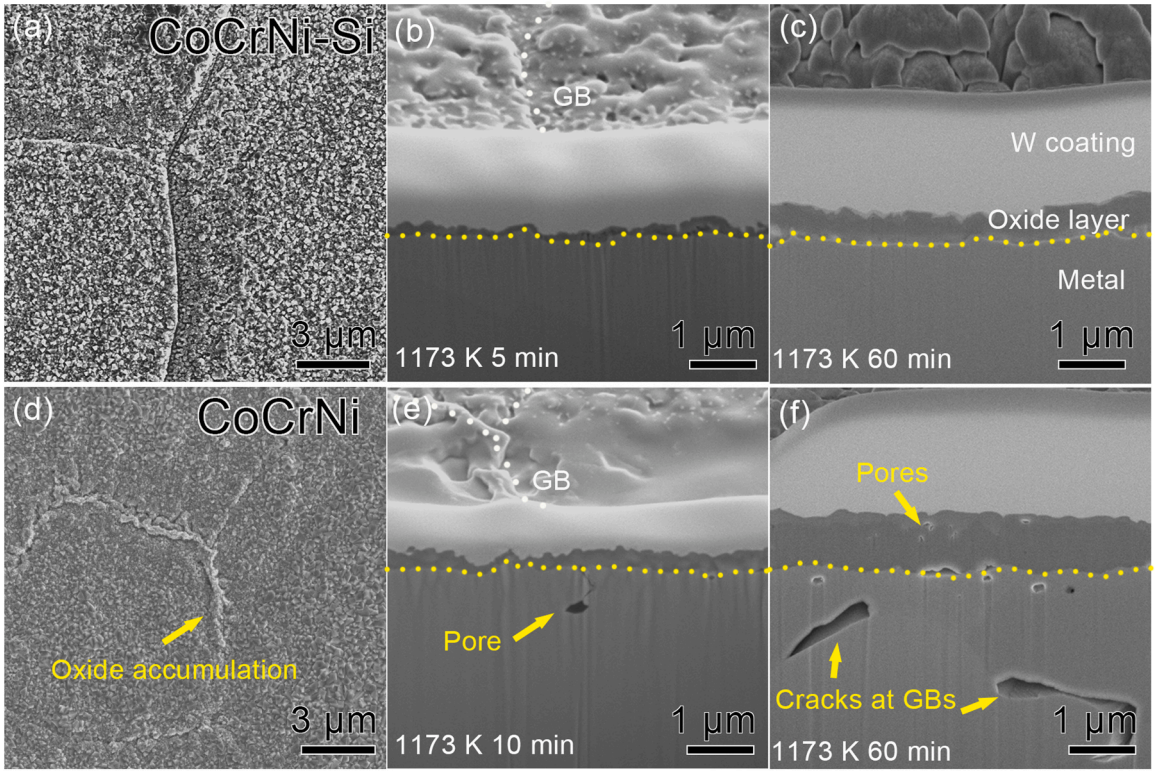

Fig. 1. Surface and cross-sectional morphology of the CoCrNi-Si (a,b, and c) and the CoCrNi (d,e, and f) alloys after oxidation treatment. The yellow dashed line indicates the interface between the oxide layer and the substrate.

thickness, with notable pores formation in the oxide layer and underlying substrate. Additionally, long intergranular cracks are visible a few microns below the surface at the grain boundaries (Fig. 1f).

To further clarify the microstructure of the layer, the oxide layer of CoCrNi-Si alloy was extracted by FIB and analyzed using transmission electron microscopy (TEM), as shown in Fig. 2. Fig. 2a presents the TEM bright-field image of the layer cross-section. It is observed that a dense layer, with a thickness ranging from 100 to 140 nm, forms on the surface of the alloy even after a brief oxidation period (1173 K, 5 min). Notably, a uniformly bright inner layer, approximately 35 nm thick, is present in the vicinity of the substrate. Upon extending the oxidation time, the bright-field image (Fig. 2b) reveals that the layer can be divided into three layers. The outermost layer is an equiaxed crystal layer with flat surfaces exposed externally. Selected-area electron diffraction (SAED) analysis (inset on the left side of Fig. 2b) indicates that this layer has a crystal structure similar to Co_3O_4. Energy dispersive spectroscopy (EDS) (Fig. 2c) confirms that this layer is rich in Cr, Co, and Ni, and the phase can be identified as $(Co, Cr, Ni)_3O_4$. The second layer of the layer is a columnar crystal layer, approximately 240 nm thick, with columnar crystals aligned along the growth direction of the oxide layer. SAED analysis (inset on the right side of Fig. 2b) and EDS (Fig. 2c) reveal that these columnar crystals are in the Cr_2O_3 phase. As shown in Fig. 2b, the innermost layer of the layer is notably bright and uniform with no visible interfaces, approximately 56 nm thick. EDS analysis (Fig. 2 cd) shows that this layer primarily consists of Si and O, with a small amount of Ni. High-resolution imaging in TEM analysis (Fig. 2e) indicates that this layer is a dense, amorphous silica tightly bonded to the crystalline layers without any visible pores. In the following sections, we will demonstrate that this amorphous layer exhibits excellent hydrogen barrier properties.

In comparison, TEM analysis of the CoCrNi alloy's oxide layer (see Supplementary Fig. 3) shows a three-layer structure. The outer layer is $(Co, Cr, Ni)_3O_4$, the middle layer consists of columnar Cr_2O_3, and the innermost layer is composed of fine equiaxed Cr_2O_3 crystals. The fine-grain structure and dispersed pores around these layers make them less tightly connected to the substrate.

Typically, the primary phase of the oxide layer, Cr_2O_3, is chemically stable and reacts slowly with dilute sulfuric acid at room temperature [28]. Therefore, the electrochemical hydrogen charging process described in this study does not lead to the complete dissolution of the oxide layer. To investigate whether the oxide layer of the alloys undergoes dissolution or damage after electrochemical hydrogen charging, the oxide layers of both alloys were characterized after hydrogen charging, as shown in Fig. 3. Fig. 3a presents a BSE-mode SEM image of the CoCrNi-Si alloy surface after hydrogen charging. At low magnification, the surface exhibits uniform contrast, indicating that despite prolonged electrochemical hydrogen charging, the oxide layer on the CoCrNi-Si alloy remains intact without significant spallation. Fig. 3b and c, captured using the ETD detector at different magnifications, reveal a dense and crack-free oxide layer with well-preserved surface details.

In contrast, as shown in Fig. 3d, the BSE-mode SEM image of the CoCrNi alloy surface after hydrogen charging displays regions with distinct contrast variations, suggesting extensive oxide layer damage. Fig. 3e provides a magnified ETD-mode SEM image of a damaged region, while Fig. 3f presents the corresponding EDS analysis. The spallation of the oxide layer is evident, with the exposed regions showing enrichment of metallic elements and a significant reduction in oxygen content, confirming complete oxide removal and direct exposure of the metallic substrate. Cracks are clearly visible on the remaining oxide layer, as indicated by the yellow arrows. Additionally, intergranular cracks are observed in the exposed metallic substrate, marked by red arrows. These observations further support the findings in Fig. 1, indicating that the adhesion strength between the oxide layer and the CoCrNi alloy substrate is relatively weak. During the hydrogen charging process, the oxide layer detaches due to factors such as bubble flow.

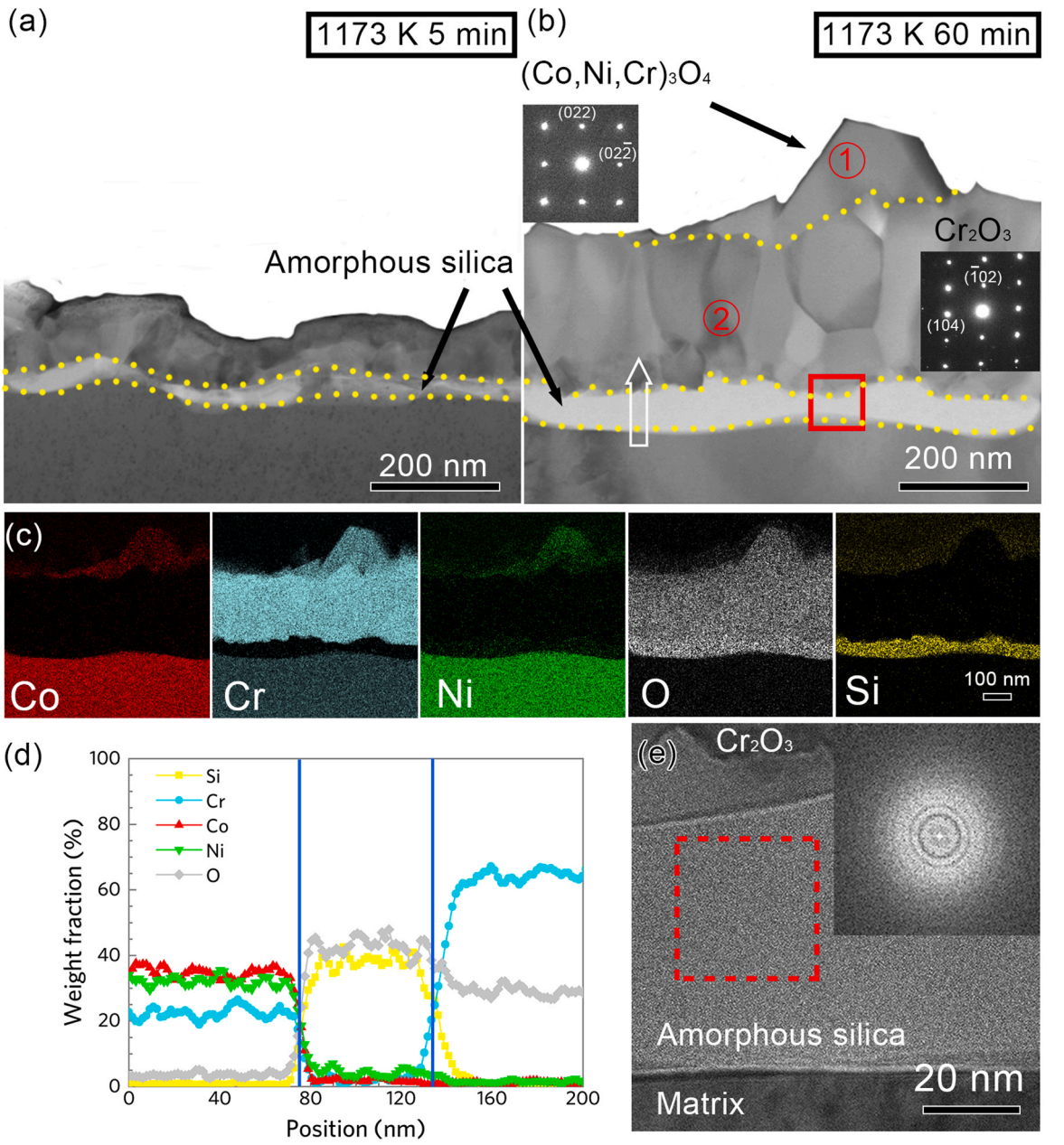

Fig. 2. TEM micrographs and EDS spectrum of the layer formed on the CoCrNi-Si alloy during oxidation treatment. (a-b) Bright-field images of short-term and long-term oxidation treatment. The SAED pattern shown in the left inset corresponds to the aperture position indicated by circle 1, while the SAED pattern in the right inset corresponds to the aperture position indicated by circle 2. The W deposition layer on the sample surface was removed through post-image processing; (c) EDS mapping of the area shown in panel b; (d) Elemental composition analysis of the area indicated by the white arrow in panel b; (e) HRTEM analysis of the area within the red box in panel b. The inset in panel e is the FFT (Fast Fourier Transform) image of the region outlined by the dashed box.

3.2. Hydrogen embrittlement resistance

Fig. 4a compares the tensile properties of CoCrNi-Si alloys with and without an AHB layer after hydrogen charging. Fig. 4b presents a comparison of the tensile properties of CoCrNi alloys, with and without a crystalline oxide layer, under identical hydrogen charging conditions. For uncharged CoCrNi-Si alloy, the yield strength is ~450 MPa, tensile strength is ~880 MPa, and the elongation after fracture reaches ~59 %. These data show little difference compared to the CoCrNi alloy, indicating that Si alloying has a limited effect on the primary mechanical properties of the alloy. After electrochemical hydrogen charging at 25 mA/cm^2 for 7 days, the elongation of bare CoCrNi-Si alloy drops to 43 %, resulting in a significant elongation loss of 25.5 %, indicating pronounced hydrogen embrittlement (hydrogen content of 23.55 wt. ppm, see Supplementary Fig. 4a). In contrast, the CoCrNi-Si alloy with an AHB layer retains an elongation of 56 % under the same hydrogen charging conditions, with a minimal elongation loss of only 2 %. TDS analysis (Supplementary Fig. 4b) shows a hydrogen content of only 8.91 wt.ppm. This demonstrates that the CoCrNi-Si alloy with an AHB layer exhibits exceptional extrinsic hydrogen embrittlement resistance.

In comparison, the CoCrNi alloy, regardless of whether it has undergone oxidation treatment, shows a significant elongation loss exceeding 25 % after hydrogen charging (Fig. 4b), indicating that the CoCrNi alloy has a high hydrogen embrittlement sensitivity, and the crystalline oxide layer does not provide effective shielding against the ingress of hydrogen.

Fig. 4c is an Ashby diagram that illustrates the performance comparison between the CoCrNi-Si alloy with an AHB layer and other major

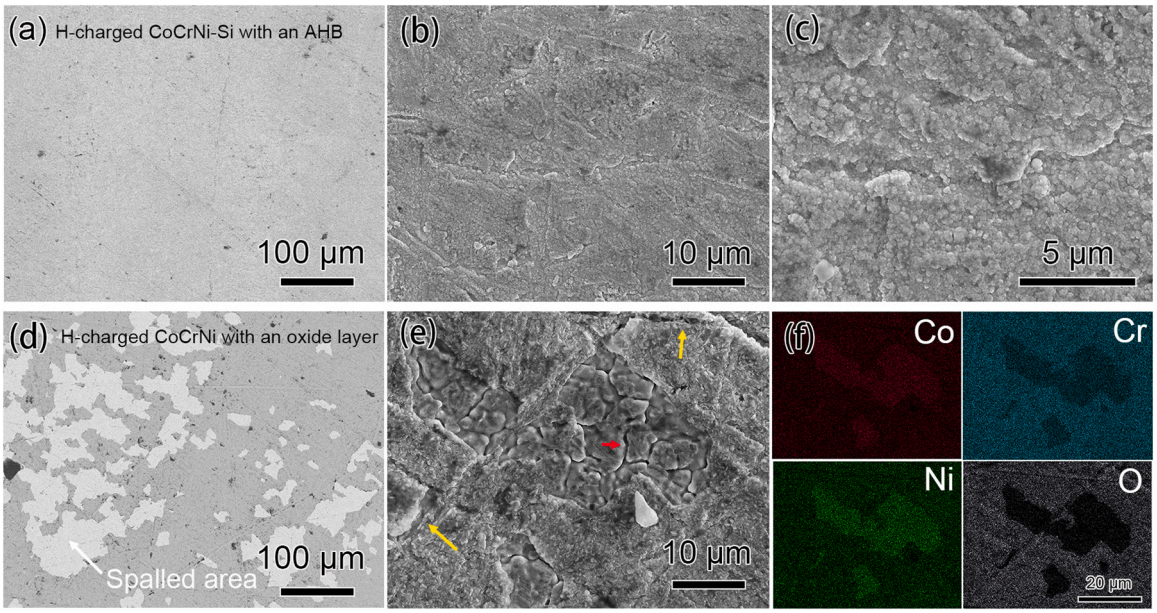

Fig. 3. SEM analysis of the surface oxide layers of the CoCrNi-Si alloy (a–c) and the CoCrNi alloy (d–f) after electrochemical hydrogen charging. (a) BSE-mode SEM image of the oxide layer on the CoCrNi-Si alloy surface; (b–c) SEM images of the oxide layer on the CoCrNi-Si alloy surface captured using an ETD detector at different magnifications; (d) BSE-mode SEM image of the oxide layer on the CoCrNi alloy surface; (e) SEM image of the damaged oxide layer on the CoCrNi alloy surface captured using an ETD detector; (f) EDS analysis of the corresponding region of (e).

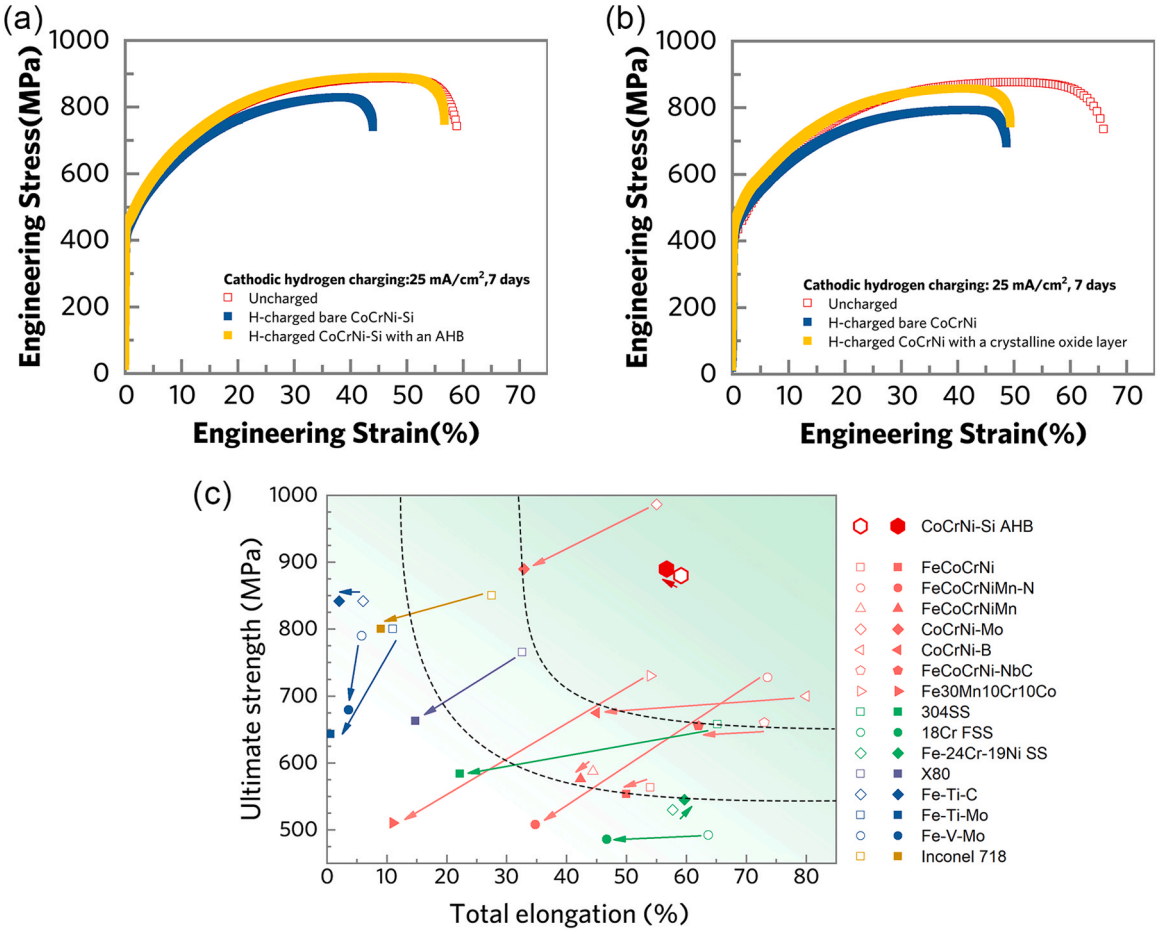

Fig. 4. (a-b) Comparison of performance before and after hydrogen charging for CoCrNi-Si and CoCrNi alloys; (c) A summary of total elongation vs. ultimate strength for various alloys with/without hydrogen. Arrows indicate the performance changes before and after hydrogen charging, with longer arrows representing more significant changes.

material classes. The tensile strength of the CoCrNi-Si alloy with an AHB layer increased from 880 MPa to 890 MPa, while the total elongation decreased from 59 % to 57 % after hydrogen charging, indicating minimal performance variation despite severe hydrogen exposure. Compared to the equiatomic alloys[24,25,29–32], stainless steels [33–35], nickel-based alloys[36], and ferritic steels[37–39] shown in the figure, this alloy shows superior extrinsic resistance to hydrogen embrittlement, highlighting the effectiveness of our approach.

To further validate the hydrogen embrittlement resistance of the alloy, we removed the AHB layer from one side of the CoCrNi-Si alloy and subsequently charged it with hydrogen. We compared the fracture morphology of the hydrogen-charged samples with and without the AHB layer, as shown in Fig. 5. The fracture surfaces of the hydrogen-charged CoCrNi-Si alloy show, from the surface to the core, a sequence of intergranular brittle fracture zones, a transitional region, and transgranular ductile fracture zones with numerous dimples. This is due to the diffusion of hydrogen from the surface to the core during electrochemical hydrogen charging, leading to a transition from ductile to brittle fracture in regions where the critical hydrogen concentration is reached. Thus, comparing the thickness of the brittle fracture zones provides additional evidence of the effectiveness of the AHB layer. As seen in Fig. 5b and c, the brittle fracture zone on the hydrogen-charged side with an AHB layer has a thickness of approximately 38.6 μm. In contrast, the brittle fracture zone on the hydrogen-charged side of the bare surface has a thickness of about 80.7 μm.

The depth of hydrogen diffusion (i.e., the thickness of the brittle layer, denoted as x) is related to the hydrogen diffusion coefficient D through the following equation:

$$x = \sqrt{6Dt} \tag{2}$$

Where x is the thickness of the brittle layer, D is the hydrogen diffusion coefficient, t is the diffusion time before fracture. The calculation shows that the diffusion coefficient on the AHB layer side is $4.106 \times 10^{-16} m^2/s$, while the diffusion coefficient on the bare surface side is $1.795 \times 10^{-15} m^2/s$. This indicates that the AHB layer provides effective hydrogen barrier performance.

To demonstrate the self-refilling characteristic of the AHB layer, we subjected both pre-oxidized and well-polished samples to extreme hydrogen gaseous charging conditions—20 MPa hydrogen gas containing trace oxygen at 573 K. As shown in Fig. 6a, the pre-oxidized and bare CoCrNi-Si alloys exhibited minimal elongation loss, approximately 13 % after exposure to high-pressure hydrogen. The fracture morphology shows a large number of ductile dimples (Fig. 6c), indicating that the fracture mode of this alloy remains ductile under these extreme conditions. In contrast, the CoCrNi alloy, regardless of pre-oxidation treatment, experienced significant deterioration in mechanical properties (Fig. 6b), with brittle fractures (Fig. 6d) occurring during the work-hardening stage. The two alloys display completely different hydrogen embrittlement behaviors under the same hydrogen charging conditions due to varying hydrogen content. The pre-oxidized and bare CoCrNi-Si alloys contain 21.23 wt.ppm and 20.22 wt.ppm of hydrogen, while the pre-oxidized and bare CoCrNi alloys have 27.76 wt.ppm and 26.49 wt. ppm, respectively (see Supplementary Fig. 5). The CoCrNi-Si alloy absorbs significantly less hydrogen, resulting in greater ductility retention. Notably, even without pre-oxidation, the CoCrNi-Si alloy maintains its hydrogen shielding capability, exhibiting hydrogen embrittlement behavior similar to pre-oxidized alloys. Thus, these results suggest that the CoCrNi-Si alloy can effectively form a self-generated AHB layer under extreme high-temperature, high-hydrogen, and corrosive conditions.

4. Discussion

Key findings in this study are as follows:

1. Si alloying does not alter the crystal structure or fundamental mechanical properties of CoCrNi alloys but significantly modifies their oxidation behavior. After short-term oxidation, CoCrNi-Si alloys develop a compact surface layer with a nanoscale amorphous silica

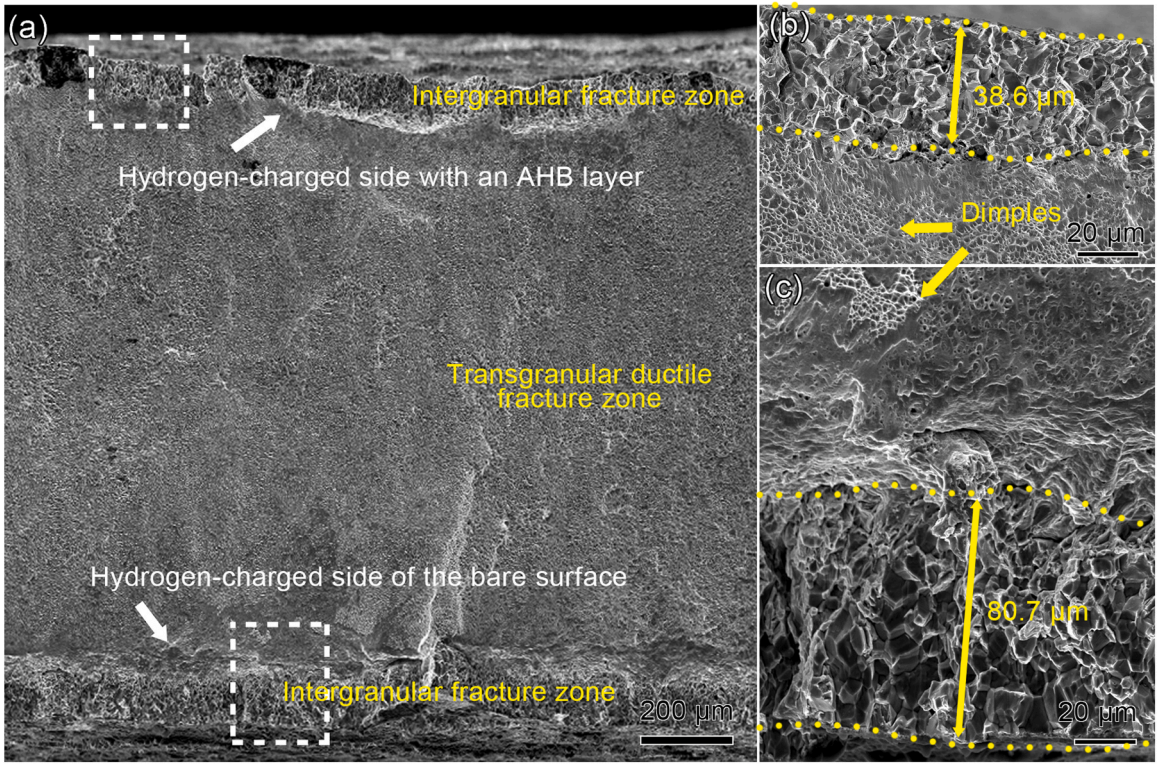

Fig. 5. Tensile fracture morphology of CoCrNi-Si samples with a single-sided amorphous hydrogen barrier.

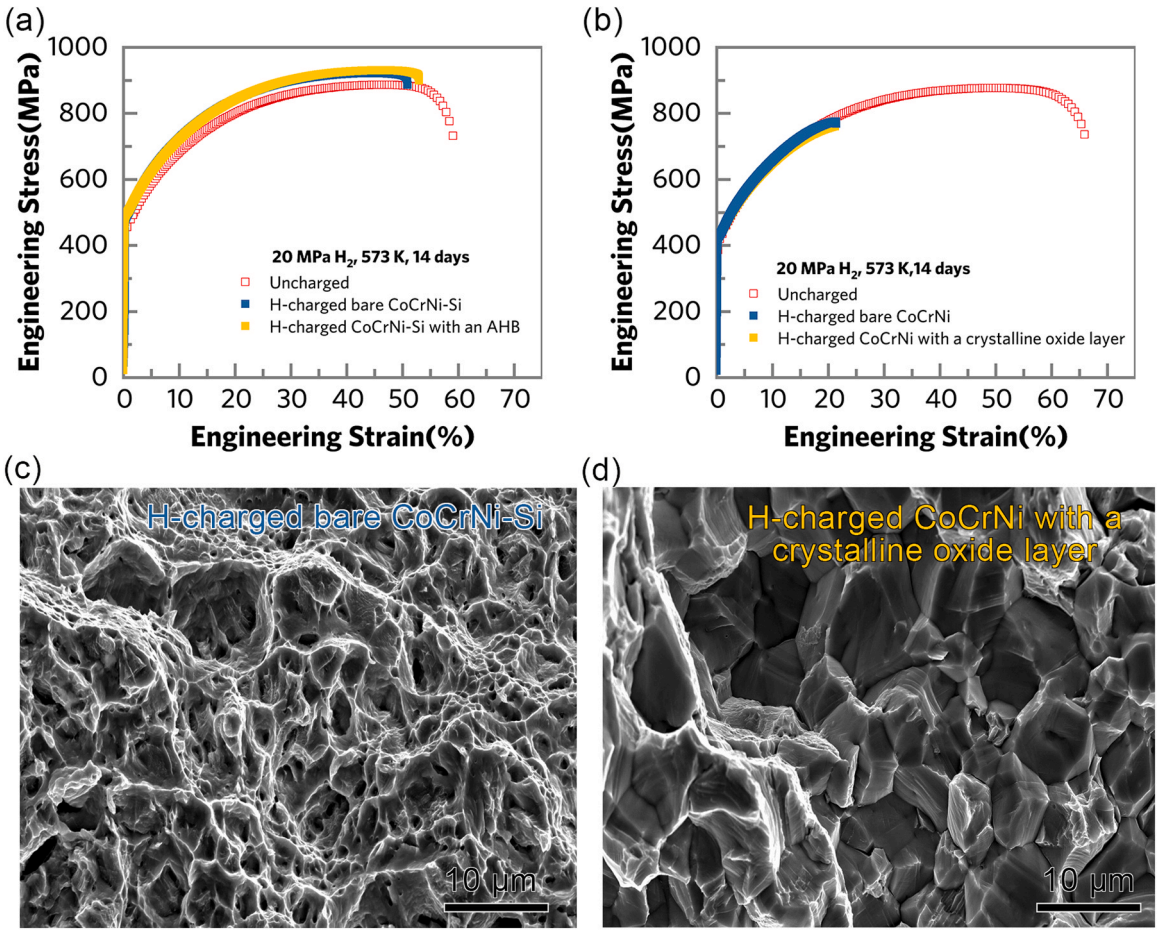

Fig. 6. (a) and (b) Mechanical property changes of the CoCrNi-(Si) alloys with and without pre-oxidation treatment after 20 MPa of impure hydrogen gas containing trace oxygen at 573 K for 14 days charging; (c) Tensile fracture morphology of hydrogen-charged bare CoCrNi-Si; (d) The fracture morphology of the CoCrNi alloy after hydrogen charging and oxidation treatment.

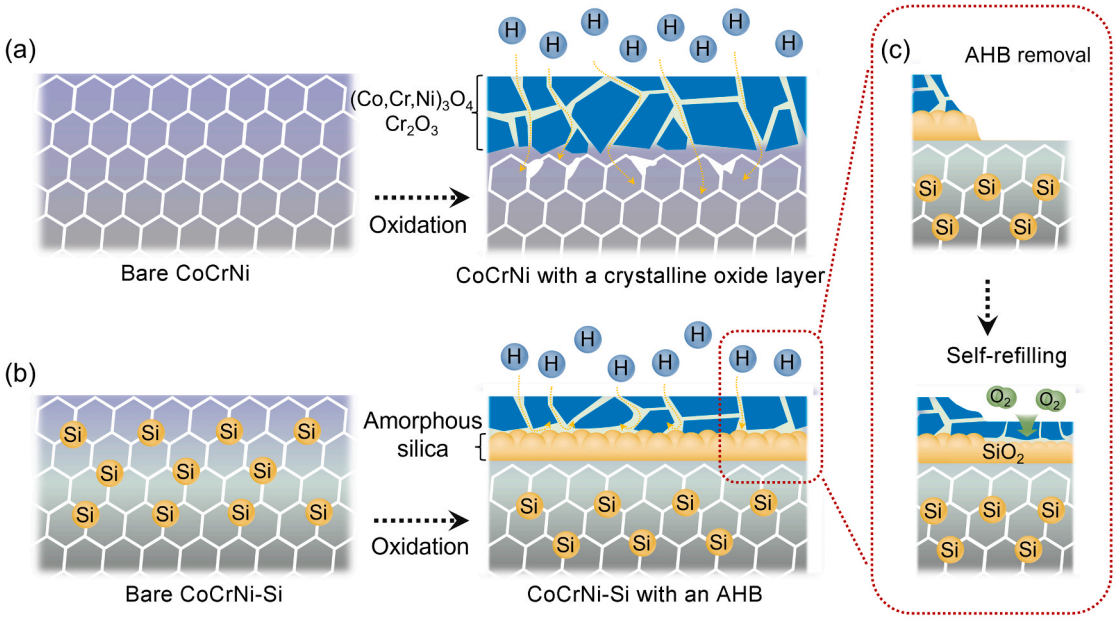

Fig. 7. Schematic of the AHB layer formation and self-refilling.

inner layer. In contrast, the oxide layer on CoCrNi alloys grows rapidly, remains porous, and lacks an amorphous inner layer.
2. The dense amorphous oxide layer on CoCrNi-Si alloys provides excellent hydrogen permeation resistance. Under identical electrochemical hydrogen charging conditions, the hydrogen uptake is reduced by 62 % compared to alloys without an oxide layer. After hydrogen charging, the loss of tensile elongation is mitigated to 2 %, and intergranular brittle fracture on the surface is significantly suppressed.
3. CoCrNi-Si alloys exhibit superior hydrogen embrittlement resistance in high-pressure, high-temperature gaseous hydrogen environments containing trace oxygen. Regardless of the presence of a preformed oxide layer, the elongation loss remains approximately 13 %, significantly lower than that of CoCrNi alloys. The hydrogen uptake in CoCrNi-Si alloys is also notably lower than in CoCrNi alloys.

Based on these findings, we propose the hydrogen embrittlement resistance mechanism of CoCrNi-Si alloys, as illustrated in Fig. 7. Unlike the ineffective and easily fractured crystalline oxide layer on CoCrNi alloys, CoCrNi-Si alloys develop a highly hydrogen-blocking and strongly bonded AHB layer with an amorphous silica inner layer. This layer spontaneously forms in critical oxygen-hydrogen environments and possesses self-refilling capability upon damage. In the following sections, we further discuss the formation mechanism of the AHB layer and its role in hydrogen resistance.

4.1. The formation mechanism of the AHB layer

The oxidation process of the CoCrNi(Si) alloys can be explained through the thermodynamics of oxidation. For the elements Co[40], Cr, and Si[41],

$$2Co(s)+O_2(g)= 2CoO(s),\ \Delta G= -472.3+ 0.145\ T \quad (3)$$

$$6CoO(s)+O_2(g)= 2Co_3O_4(s),\ \Delta G= -392.02+ 0.318T \quad (4)$$

$$4/3Cr(s)+O_2(g)= 2/3Cr_2O_3(s),\ \Delta G= -773.17+ 0.148T \quad (5)$$

$$Si(s)+O_2(g)=SiO_2(s),\ \Delta G= -907.1+ 0.175T \quad (6)$$

Based on the thermodynamic calculations, at 900°C, the following Gibbs free energy values are obtained: $\Delta G_{CoO} = -302.2$ kJ/mol, $\Delta G_{CoO\text{-}Co3O4} = -19.0$ kJ/mol, $\Delta G_{Cr2O3} = -599.6$ kJ/mol, and $\Delta G_{SiO2} = -701.8$ kJ/mol. These values indicate that SiO_2 forms preferentially, followed by Cr_2O_3, and finally Co oxidation, which stabilizes as Co_3O_4. This preferential formation of SiO_2 followed by Cr_2O_3 has also been observed in FeCrSi and FeNiCr-Si systems[42].

The diffusion coefficients of various elements in alloys follow the Arrhenius law. At 900°C, the diffusion coefficients are as follows [43–45]: $D_{Cr\ in\ CoCrNi}=1.616\times 10^{-9}m^2/s$; $D_{Ni\ in\ CoCrNi}=4.713\times 10^{-10}m^2/s$; $D_{Co\ in\ CoCrNi}=2.789\times 10^{-9}m^2/s$, $D_{Si\ in\ Ni}= 8.948\times 10^{-16}m^2/s$, $D_{O\ in\ Ni}=2.293\times 10^{-10}m^2/s$. At 1173 K, the diffusion rates of Cr and Co in CoCrNi alloys are higher than that of oxygen. This indicates that Cr and Co elements are more prone to diffuse to the surface and react with oxygen, leading to external oxidation. In contrast, Si does not readily diffuse to the surface. Instead, oxygen diffuses into the substrate and reacts with Si to form an internal amorphous SiO_2 layer.

Thus, in alloys without Si, the rapid external oxidation of Cr and Co leads to significant depletion of these elements in the subsurface. Notably, grain boundaries, acting as rapid diffusion pathways, facilitate even faster depletion of Cr. The rapid loss of these elements results in the accumulation of vacancies in the subsurface, leading to the formation of pores (Supplementary Fig. 3).

In contrast, for Si-containing alloys, the initial internal oxidation forms an amorphous SiO_2 layer, which lacks rapid diffusion pathways and effectively suppresses the diffusion of Cr and Co to the surface, thereby mitigating the formation of pores caused by the Kirkendall effect [46]. Consequently, the oxide layer in the CoCrNi-Si alloy is thinner, denser, and more strongly bonded to the substrate.

4.2. The hydrogen barrier mechanism of the AHB layer

The hydrogen diffusion rate in CoCrNi alloy at room temperature is estimated to be $2.086\times 10^{-15}m^2/s$, as calculated using Eq. 2 and the brittle layer thickness shown in Supplementary Fig. 6. In contrast, the hydrogen diffusion rate in single-crystal Cr_2O_3 at room temperature is significantly lower, $8.41\times 10^{-22}m^2/s$[47], which should bring a remarkable enhancement in hydrogen resistance compared to CoCrNi alloy. However, the findings of this study show that Cr_2O_3 layer on the CoCrNi alloy surface does not provide effective hydrogen resistance. In contrast, the AHB layer formed on the surface of the Si-alloyed variant exhibits superior hydrogen resistance compared to conventional oxide layers. The primary mechanisms for this improvement are twofold:

First, the inner amorphous silica layer inhibits Cr diffusion toward the surface, preventing void formation caused by the Kirkendall effect [46] and ensuring a dense and strongly bonded oxide layer (see Fig. 1 and Fig. 2). The comparison of oxide layer morphologies after hydrogen charging indicates that the AHB layer on the Si-alloyed surface remains intact even after prolonged bubble flushing during the process (Fig. 3a–c), demonstrating long-term protective capability. In contrast, the oxide layer on the CoCrNi alloy lacks an inner amorphous silica layer to regulate Cr diffusion toward the surface, resulting in a rapid thickening of the oxide layer, which becomes porous, loosely bonded to the substrate, and prone to spalling during hydrogen charging, ultimately losing its protective function (Fig. 3b–f). Additionally, the excessively fast-growing oxide layer depletes Cr in the near-surface metallic matrix, particularly at grain boundaries, leading to intergranular voids (Fig. 1 and Supplementary Fig. 3), which further compromise the alloy's resistance to hydrogen embrittlement[23]. Therefore, although Cr_2O_3 itself has some hydrogen-blocking capability, it is less effective than the AHB.

Second, the inner amorphous silica layer itself exhibits excellent hydrogen-blocking capability. The hydrogen diffusion rate in the amorphous silica layer is inherently low. The diffusion rate of hydrogen (H) atoms in defect-rich amorphous SiO_2 is given by [48]::

$$D_{Hin\ SiO2} = 5.079\times 10^{-12}\exp^{-\frac{50155}{RT}} \quad (7)$$

At room temperature, this results in a diffusion rate of $8.205\times 10^{-21}m^2/s$. This low diffusion rate is due to hydrogen forming permanent hydroxyl groups (OH-) with oxygen in amorphous SiO_2, a process facilitated by hydrogen bonding. The presence of defects in the amorphous SiO_2 leads to an increase in oxygen free radicals and dangling bonds, enhancing its ability to capture hydrogen and retarding its diffusion [48]. As shown in the EDS analysis results in Fig. 2, some metal elements, such as Ni, are dissolved in the amorphous silica layer. According to the study by Yang et al. [49], the presence of metals like Ni in amorphous SiO_2 introduces additional oxygen free radicals, further enhancing hydrogen capture and slowing diffusion. Moreover, the dense amorphous silica inner layer, which lacks rapid hydrogen diffusion pathways such as grain boundaries and dislocations, can effectively exhibit its high hydrogen barrier capability. In contrast, the columnar Cr_2O_3 grains in the oxide layer contain grain boundaries that act as rapid transport pathways for hydrogen, leading to a much higher diffusion rate than that reported for single-crystal Cr_2O_3 [47]. Consequently, its hydrogen-blocking performance is relatively poor.

5. Conclusion

This study investigates the hydrogen embrittlement behavior and microstructural evolution of the CoCrNi-Si and CoCrNi alloys before and after oxidation. A novel hydrogen embrittlement resistance strategy is proposed, which significantly enhances the extrinsic hydrogen

resistance of equiatomic CoCrNi alloys.

1. During the oxidation of CoCrNi-Si alloys, thermodynamic factors and differences in elemental diffusion rates lead to the formation of a dense, nanoscale amorphous silica layer near the metal substrate. Due to the absence of rapid diffusion pathways, this amorphous inner layer inhibits the outward diffusion of Cr from the substrate, thereby suppressing oxide layer growth and preventing the Kirkendall effect. As a result, the oxide layer on CoCrNi-Si alloys is significantly denser and more stable.
2. The dense and strongly bonded nature of the amorphous silica layer, combined with the absence of rapid hydrogen diffusion pathways, provides exceptional hydrogen resistance. After prolonged hydrogen charging at 25 mA/cm^2 in sulfuric acid for 7 days, the hydrogen uptake in CoCrNi-Si alloys is reduced by 62 % compared to unoxidized alloys. Even under severe hydrogen exposure, the alloy retains a high tensile strength of 890 MPa and an excellent elongation of 57 %, with elongation loss mitigated to only 4 % (down from over 25 % initially), demonstrating remarkable resistance to hydrogen embrittlement. Under 20 MPa hydrogen gas with trace oxygen at 573 K for 14 days, the bare CoCrNi-Si alloy exhibits an elongation loss of only 13 %, in stark contrast to the 67 % elongation loss observed in CoCrNi alloys.

CRediT authorship contribution statement

Wang Shuai: Writing – original draft, Supervision, Funding acquisition, Formal analysis, Data curation, Conceptualization. **Yang Mujin:** Investigation, Funding acquisition. **Zhu Dingding:** Investigation. **Du Bo:** Investigation. **He Minglin:** Investigation, Funding acquisition. **Zhang Shuting:** Writing – original draft, Visualization, Investigation, Data curation. **Yi Jiang:** Writing – original draft, Visualization, Methodology, Investigation, Funding acquisition, Formal analysis, Data curation, Conceptualization.

Declaration of Competing Interest

The authors declare that they have no known competing financial interests or personal relationships that could have appeared to influence the work reported in this paper.

Acknowledgements

This work is financially supported by the National Key R&D Program of China (2022YFB4600700) and National Natural Science Foundation of China (52475364 and 52301154). J. Y. and S. W. acknowledge the support from the Shenzhen Science and Technology Program through the grants (JCYJ20220530114400001 and JCYJ20210324104414040). J. Y. and M. Y. acknowledge the support from the Guangdong Basic and Applied Basic Research Foundation through the grants (2024A1515010358 and 2023A1515240048). M. H. acknowledges the support from the Guangdong Provincial Department of Education University Youth Innovative Talent Research Project through the grant (2023KQNCX066). All authors gratefully acknowledge the assistance from Dr. Yang Qiu and Dr. Dongsheng He at SUStech Core Research Facilities. We thank the electron microscope center of KAIPLE Co. Ltd. (Changsha) for the support of microstructural characterizations.

Data availability

Data will be made available on request.

References

[1] S.J. Zinkle, G.S. Was, Materials challenges in nuclear energy, Acta Mater. 61 (2013) 735–758, https://doi.org/10.1016/j.actamat.2012.11.004.
[2] B. Sun, W. Lu, B. Gault, R. Ding, S.K. Makineni, D. Wan, C.-H. Wu, H. Chen, D. Ponge, D. Raabe, Chemical heterogeneity enhances hydrogen resistance in high-strength steels, Nat. Mater. 20 (2021) 1629–1634, https://doi.org/10.1038/s41563-021-01050-y.
[3] I.M. Robertson, P. Sofronis, A. Nagao, M.L. Martin, S. Wang, D.W. Gross, K. E. Nygren, Hydrogen Embrittlement Understood, Metall. Mater. Trans. A 46 (2015) 2323–2341, https://doi.org/10.1007/s11661-015-2836-1.
[4] Y.-S. Chen, H. Lu, J. Liang, A. Rosenthal, H. Liu, G. Sneddon, I. McCarroll, Z. Zhao, W. Li, A. Guo, J.M. Cairney, Observation of hydrogen trapping at dislocations, grain boundaries, and precipitates, Science 367 (2020) 171–175, https://doi.org/10.1126/science.aaz0122.
[5] H. Zhao, P. Chakraborty, D. Ponge, T. Hickel, B. Sun, C.-H. Wu, B. Gault, D. Raabe, Hydrogen trapping and embrittlement in high-strength Al alloys, Nature 602 (2022) 437–441, https://doi.org/10.1038/s41586-021-04343-z.
[6] X. Li, X. Ma, J. Zhang, E. Akiyama, Y. Wang, X. Song, Review of Hydrogen Embrittlement in Metals: Hydrogen Diffusion, Hydrogen Characterization, Hydrogen Embrittlement Mechanism and Prevention, Acta Metall. Sin. (Engl. Lett. 33 (2020) 759–773, https://doi.org/10.1007/s40195-020-01039-7.
[7] M. Koyama, E. Akiyama, K. Tsuzaki, Hydrogen embrittlement in a Fe–Mn–C ternary twinning-induced plasticity steel, Corros. Sci. 54 (2012) 1–4, https://doi.org/10.1016/j.corsci.2011.09.022.
[8] L. Liu, K. Tanaka, A. Hirose, K. Kobayashi, Effects of precipitation phases on the hydrogen embrittlement sensitivity of Inconel 718, Sci. Technol. Adv. Mater. 3 (2002) 335–344, https://doi.org/10.1016/S1468-6996(02)00039-6.
[9] D. Levchuk, F. Koch, H. Maier, H. Bolt, Deuterium permeation through Eurofer and α-alumina coated Eurofer, J. Nucl. Mater. 328 (2004) 103–106, https://doi.org/10.1016/j.jnucmat.2004.03.008.
[10] D. Figueroa, M.J. Robinson, The effects of sacrificial coatings on hydrogen embrittlement and re-embrittlement of ultra high strength steels, Corros. Sci. 50 (2008) 1066–1079, https://doi.org/10.1016/j.corsci.2007.11.023.
[11] P. Zhou, W. Li, X. Zhu, Y. Li, X. Jin, J. Chen, Graphene Containing Composite Coatings as a Protective Coatings against Hydrogen Embrittlement in Quenching & Partitioning High Strength Steel, J. Electrochem. Soc. 163 (2016) D160, https://doi.org/10.1149/2.0551605jes.
[12] K. Saito, S. Inayoshi, Y. Ikeda, Y. Yang, S. Tsukahara, TiN thin film on stainless steel for extremely high vacuum material, J. Vac. Sci. Technol. A 13 (1995) 556–561, https://doi.org/10.1116/1.579785.
[13] T. Michler, Influence of plasma nitriding on hydrogen environment embrittlement of 1.4301 austenitic stainless steel, Surf. Coat. Technol. 202 (2008) 1688–1695, https://doi.org/10.1016/j.surfcoat.2007.07.036.
[14] X. Liu, W. Xie, W. Chen, H. Zhang, Effects of grain boundary and boundary inclination on hydrogen diffusion in α-iron, J. Mater. Res. 26 (2011) 2735–2743, https://doi.org/10.1557/jmr.2011.262.
[15] Z. Li, K.G. Pradeep, Y. Deng, D. Raabe, C.C. Tasan, Metastable high-entropy dual-phase alloys overcome the strength–ductility trade-off, Nature 534 (2016) 227–230, https://doi.org/10.1038/nature17981.
[16] B. Gludovatz, A. Hohenwarter, D. Catoor, E.H. Chang, E.P. George, R.O. Ritchie, A fracture-resistant high-entropy alloy for cryogenic applications, Science 345 (2014) 1153–1158, https://doi.org/10.1126/science.1254581.
[17] Q. Pan, L. Zhang, R. Feng, Q. Lu, K. An, A.C. Chuang, J.D. Poplawsky, P.K. Liaw, L. Lu, Gradient cell–structured high-entropy alloy with exceptional strength and ductility, Science 374 (2021) 984–989, https://doi.org/10.1126/science.abj8114.
[18] Y. Yao, Z. Huang, P. Xie, S.D. Lacey, R.J. Jacob, H. Xie, F. Chen, A. Nie, T. Pu, M. Rehwoldt, D. Yu, M.R. Zachariah, C. Wang, R. Shahbazian-Yassar, J. Li, L. Hu, Carbothermal shock synthesis of high-entropy-alloy nanoparticles, Science 359 (2018) 1489–1494, https://doi.org/10.1126/science.aan5412.
[19] L. Han, F. Maccari, I.R. Souza Filho, N.J. Peter, Y. Wei, B. Gault, O. Gutfleisch, Z. Li, D. Raabe, A mechanically strong and ductile soft magnet with extremely low coercivity, Nature 608 (2022) 310–316, https://doi.org/10.1038/s41586-022-04935-3.
[20] K.-Y. Tsai, M.-H. Tsai, J.-W. Yeh, Sluggish diffusion in Co–Cr–Fe–Mn–Ni high-entropy alloys, Acta Mater. 61 (2013) 4887–4897, https://doi.org/10.1016/j.actamat.2013.04.058.
[21] C.K. Soundararajan, H. Luo, D. Raabe, Z. Li, Hydrogen resistance of a 1 GPa strong equiatomic CoCrNi medium entropy alloy, Corros. Sci. 167 (2020) 108510, https://doi.org/10.1016/j.corsci.2020.108510.
[22] H. Luo, S.S. Sohn, W. Lu, L. Li, X. Li, C.K. Soundararajan, W. Krieger, Z. Li, D. Raabe, A strong and ductile medium-entropy alloy resists hydrogen embrittlement and corrosion, Nat. Commun. 11 (2020) 3081, https://doi.org/10.1038/s41467-020-16791-8.
[23] Q. Li, J.W. Mo, S.H. Ma, F.H. Duan, Y.L. Zhao, S.F. Liu, W.H. Liu, S.J. Zhao, C. T. Liu, P.K. Liaw, T. Yang, Defeating hydrogen-induced grain-boundary embrittlement via triggering unusual interfacial segregation in FeCrCoNi-type high-entropy alloys, Acta Mater. 241 (2022) 118410, https://doi.org/10.1016/j.actamat.2022.118410.
[24] H. Chen, Y. Ma, C. Li, Q. Zhao, Y. Huang, H. Luo, H. Ma, X. Li, A nano-sized NbC precipitation strengthened FeCoCrNi high entropy alloy with superior hydrogen embrittlement resistance, Corros. Sci. 208 (2022) 110636, https://doi.org/10.1016/j.corsci.2022.110636.
[25] H. Luo, Z. Li, D. Raabe, Hydrogen enhances strength and ductility of an equiatomic high-entropy alloy, Sci. Rep. 7 (2017) 9892, https://doi.org/10.1038/s41598-017-10774-4.

[26] S. Liu, W. Lin, Y. Zhao, D. Chen, G. Yeli, F. He, S. Zhao, J. Kai, Effect of silicon addition on the microstructures, mechanical properties and helium irradiation resistance of NiCoCr-based medium-entropy alloys, J. Alloy. Compd. 844 (2020) 156162, https://doi.org/10.1016/j.jallcom.2020.156162.
[27] H. Chang, T.W. Zhang, S.G. Ma, D. Zhao, R.L. Xiong, T. Wang, Z.Q. Li, Z.H. Wang, Novel Si-added CrCoNi medium entropy alloys achieving the breakthrough of strength-ductility trade-off, Mater. Des. 197 (2021) 109202, https://doi.org/10.1016/j.matdes.2020.109202.
[28] G.B. Reartes, P.J. Morando, M.A. Blesa, P.B. Hewlett, E. Matijevic, Reactivity of Chromium Oxide in Aqueous Solutions. 2. Acid Dissolution, Langmuir 11 (1995) 2277–2284, https://doi.org/10.1021/la00006a068.
[29] J. Yi, X. Zhuang, J. He, M. He, W. Liu, S. Wang, Effect of Mo doping on the gaseous hydrogen embrittlement of a CoCrNi medium-entropy alloy, Corros. Sci. 189 (2021) 109628, https://doi.org/10.1016/j.corsci.2021.109628.
[30] K.E. Nygren, S. Wang, K.M. Bertsch, H. Bei, A. Nagao, I.M. Robertson, Hydrogen embrittlement of the equi-molar FeNiCoCr alloy, Acta Mater. 157 (2018) 218–227, https://doi.org/10.1016/j.actamat.2018.07.032.
[31] X. Li, J. Yin, J. Zhang, Y. Wang, X. Song, Y. Zhang, X. Ren, Hydrogen embrittlement and failure mechanisms of multi-principal element alloys: A review, J. Mater. Sci. Technol. 122 (2022) 20–32, https://doi.org/10.1016/j.jmst.2022.01.008.
[32] K. Ichii, M. Koyama, C.C. Tasan, K. Tsuzaki, Comparative study of hydrogen embrittlement in stable and metastable high-entropy alloys, Scr. Mater. 150 (2018) 74–77, https://doi.org/10.1016/j.scriptamat.2018.03.003.
[33] Y. Zhao, D.-H. Lee, M.-Y. Seok, J.-A. Lee, M.P. Phaniraj, J.-Y. Suh, H.-Y. Ha, J.-Y. Kim, U. Ramamurty, J. Jang, Resistance of CoCrFeMnNi high-entropy alloy to gaseous hydrogen embrittlement, Scr. Mater. 135 (2017) 54–58, https://doi.org/10.1016/j.scriptamat.2017.03.029.
[34] E. Malitckii, Y. Yagodzinskyy, P. Lehto, H. Remes, J. Romu, H. Hänninen, Hydrogen effects on mechanical properties of 18%Cr ferritic stainless steel, Mater. Sci. Eng.: A 700 (2017) 331–337, https://doi.org/10.1016/j.msea.2017.06.028.
[35] Y. Ogawa, H. Hosoi, K. Tsuzaki, T. Redarce, O. Takakuwa, H. Matsunaga, Hydrogen, as an alloying element, enables a greater strength-ductility balance in an Fe-Cr-Ni-based, stable austenitic stainless steel, Acta Mater. 199 (2020) 181–192, https://doi.org/10.1016/j.actamat.2020.08.024.
[36] X. Lu, Y. Ma, D. Wang, On the hydrogen embrittlement behavior of nickel-based alloys: Alloys 718 and 725, Mater. Sci. Eng.: A 792 (2020) 139785, https://doi.org/10.1016/j.msea.2020.139785.
[37] P. Gong, A. Turk, J. Nutter, F. Yu, B. Wynne, P. Rivera-Diaz-del-Castillo, W. M. Rainforth, Hydrogen embrittlement mechanisms in advanced high strength steel, Acta Mater. 223 (2022) 117488, https://doi.org/10.1016/j.actamat.2021.117488.
[38] T. Depover, K. Verbeken, The effect of TiC on the hydrogen induced ductility loss and trapping behavior of Fe-C-Ti alloys, Corros. Sci. 112 (2016) 308–326, https://doi.org/10.1016/j.corsci.2016.07.013.
[39] Z. Pu, Y. Chen, L.H. Dai, Strong resistance to hydrogen embrittlement of high-entropy alloy, Mater. Sci. Eng.: A 736 (2018) 156–166, https://doi.org/10.1016/j.msea.2018.08.101.
[40] K.C. Sabat, R.K. Paramguru, S. Pradhan, B.K. Mishra, Reduction of Cobalt Oxide (Co3O4) by Low Temperature Hydrogen Plasma, Plasma Chem. Plasma Process. 35 (2015) 387–399, https://doi.org/10.1007/s11090-014-9602-9.
[41] J. Lim, Eff. Chromium Silicon Corros. iron Alloy. Lead. -bismuth eutectic, Mass. Inst. Technol. (2006).
[42] Z. Xu, L. Song, Y. Zhao, S. Liu, The formation mechanism and effect of amorphous SiO2 on the corrosion behaviour of Fe-Cr-Si ODS alloy in LBE at 550 °C, Corros. Sci. 190 (2021) 109634, https://doi.org/10.1016/j.corsci.2021.109634.
[43] M. David, A. Prillieux, D. Monceau, D. Connétable, First-principles study of the insertion and diffusion of interstitial atoms (H, C, N and O) in nickel, J. Alloy. Compd. 822 (2020) 153555, https://doi.org/10.1016/j.jallcom.2019.153555.
[44] T. Garnier, V.R. Manga, P. Bellon, D.R. Trinkle, Diffusion of Si impurities in Ni under stress: A first-principles study, Phys. Rev. B 90 (2014) 024306, https://doi.org/10.1103/PhysRevB.90.024306.
[45] S. Zhao, Y. Osetsky, Y. Zhang, Preferential diffusion in concentrated solid solution alloys: NiFe, NiCo and NiCoCr, Acta Mater. 128 (2017) 391–399, https://doi.org/10.1016/j.actamat.2017.01.056.
[46] A. Paul, M.J.H. van Dal, A.A. Kodentsov, F.J.J. van Loo, The Kirkendall effect in multiphase diffusion, Acta Mater. 52 (2004) 623–630, https://doi.org/10.1016/j.actamat.2003.10.007.
[47] C. Chen, H. Yu, S. Zheng, First-principles study of hydrogen diffusion mechanism in Cr2O3, Sci. China Technol. Sci. 54 (2011) 88–94, https://doi.org/10.1007/s11431-010-4112-3.
[48] D. Fink, J. Krauser, D. Nagengast, T.A. Murphy, J. Erxmeier, L. Palmetshofer, D. Bräunig, A. Weidinger, Hydrogen implantation and diffusion in silicon and silicon dioxide, Appl. Phys. A 61 (1995) 381–388, https://doi.org/10.1007/BF01540112.
[49] P. Yang, C.F. Song, M.K. Lü, J. Chang, Y.Z. Wang, Z.X. Yang, G.J. Zhou, Z.P. Ai, D. Xu, D.L. Yuan, Defects and Photoluminescence of Ni2+ and Mn2+ -Doped Sol–Gel SiO2 Glass, J. Solid State Chem. 160 (2001) 272–277, https://doi.org/10.1006/jssc.2001.9245.